ORIGINAL PAPER

High frequency-based protection algorithm for meshed MTDC systems

Ahmed E. B. Abu-Elanien[1] · Ahmed A. Elserougi[1]

Abstract

This research presents a high frequency-based algorithm for zonal protection of meshed Multi-Terminal high voltage Direct Current (MTDC) systems. Discrete wavelet transform (DWT) is used to capture high frequency current transients from one end of each line. The faulty line is identified by analyzing two distinct high frequency bands form the captured transients. The characteristics of these current transients during normal condition are different from faulty condition. A four-terminal meshed MTDC model is used to test the performance of the protection algorithm. Various faults with different fault scenarios were simulated using four-terminal meshed MTDC model. The simulation results showed success of the algorithm in identifying internal faults. Moreover, the high frequency algorithm showed robustness against other abnormal conditions such as AC faults and sudden change of wind power.

Keywords Protection · Multi-terminal · MTDC · Wavelets · Wind farms

1 Introduction

Generation of clean energy and reduction of toxic emissions of conventional generation are growing concerns worldwide. Wind farms' installations are growing due to their ability to generate significant amount of clean energy. Multi-Terminal high voltage Direct Current (MTDC) systems facilitate the interconnection between multiple AC grids and wind farms [1]. Moreover, MTDC systems are ideal for connecting multiple distant AC systems [1]. Voltage-source converters (VSC) have proven its superiority over line-commutated converters (LCC) for high-voltage direct current (HVDC) applications [2, 3]. VSC-MTDC has faster dynamic response, no commutation failures, independent control of active and reactive powers, and ability to connect to weak grids [2, 3]. Therefore, future installations of MTDC are expected to depend mainly on VSC technology. Wind farms' generated power can be delivered to multiple existing distant AC systems via VSC-MTDC technology [4, 5].

Although MTDC systems have numerous benefits for transmission of electrical power, DC faults generate extremely high current at very short time due to discharge of converters' coupling capacitors. This fault current may

damage semiconductor devices of the terminal converters if not cleared quickly [1]. Therefore, protection of MTDC systems is a challenging task since it needs very fast detection and clearance of faults.

A distance protection technique is proposed in Ref. [6]; however, this technique was not tested for real size systems. It was tested on 1 km, 1 kV transmission line which is not realistic. Moreover, the presented distance protection method suffers from inaccurate fault distance for faults with low fault resistance (5 Ω). These restrictions may limit its application on real systems. Cable faults in MTDC systems were detected using discrete wavelet transform (DWT) in Ref. [7, 8]. The algorithm presented in Ref. [7] used initial variation of DWT coefficients for voltage and current, and voltage derivative to identify internal faults in cable-based MTDC system. Nevertheless, the wavelet coefficients for faulty and unfaulty cables jump abruptly immediately after the fault, which may cause overlapping between internal and external faults. Instead of using the values of the wavelet coefficients, spectral energy gives better insight about the wavelet coefficients. Moreover, multiple faults with different locations and fault resistances were not tested. Boundary wavelet transform was used in Ref. [8] for protection of MTDC. Nonetheless, this paper showed problems in internal fault identification for faults with fault resistance. Moreover, the methods presented in Ref. [7, 8] were tested on cable-based MTDC systems, they were not verified for overhead lines.

✉ Ahmed E. B. Abu-Elanien
    ahmed.abuelanien@alexu.edu.eg

[1] Electrical Engineering Department, Faculty of Engineering, Alexandria University, Alexandria 21544, Egypt

Double-end transient-based methods are presented in Ref. [9–11]. The transient current components at both line ends are used to identify internal faults. However, they need high-speed communication system, which affects system reliability, and adds to the installation cost. Moreover, the relaying times for these algorithms are 3 ms or more due to communication delay specially for long lines. Traveling waves-based methods were presented in Refs. [12, 13]. These methods depend on recording the arrival times of fault surges at different locations to identify fault location. Yet, these methods need fast and complex communication between all measurement units. Moreover, they need very high sampling frequency to provide acceptable performance, which complicates the practical implementation of these algorithms. Furthermore, the propagation delay of the communication signals specially for long-lines MTDC systems increases the relaying time of the relay which is very important design factor. A transient current-based protection technique was presented in Ref. [14]. Nevertheless, it is designed for HVDC lines with line commutated converters, which have different transient fault characteristics compared with VSC-MTDC. Naïve Bayes classifier was used to identify internal faults using local measurements of voltage and currents in Ref. [15]. However, Naïve Bayes classification system depends mainly on probability; accordingly, there is a gray zone in which the fault cannot be classified with 100% dependability. Moreover, faults with fault resistance higher than 10 Ω were not tested. Different protection algorithms were proposed in Ref. [16–19] for protection of radial MTDC systems. However, they are not tested on meshed systems.

This paper presents a single ended protection algorithm for meshed MTDC systems. The algorithm depends on captured high frequency transients at one line end to identify internal faults. This protection algorithm is designed to overcome the shortcomings of the research indicated in the literature survey. The high frequency-based algorithm has the following advantages:

1. It is based on data captured from one line end; therefore, it does not need long communication channels. Accordingly, the protection system is cheaper, more reliable, and less complex.
2. It performs very well for faults at different distances, fault resistances, and fault inception times.
3. The trip signal takes only 1 ms to be issued for internal faults, which is very fast relaying time. This time guarantees protection of converters' semiconductor devices from damage due to the high initial fault current.
4. The used sampling frequency is 100 kHz which is not too high to be realized. Therefore, the implementation of the high frequency algorithm presented in this research is anticipated to be feasible using current hardware platforms.
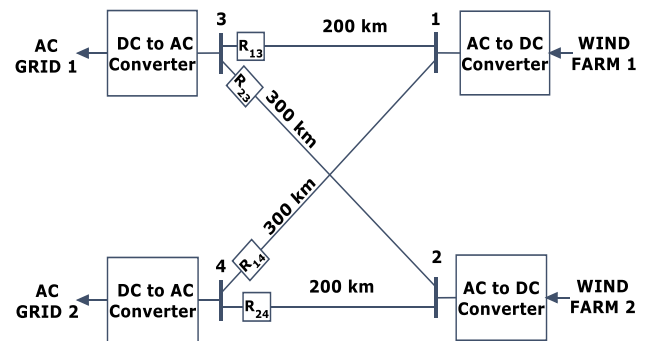

Fig. 1 Meshed power system model

5. The protection algorithm is tested for different abnormal conditions such AC faults and sudden change in the wind power injection. Many current protection techniques did not include relay response under non-fault abnormalities.

2 MTDC model

Figure 1 shows a four-terminal meshed bipolar MTDC system which connects two AC grids with two wind farms via four overhead lines. The voltage level is 500 kV ($\pm$ 250 kV). The line lengths are shown on Fig. 1. The resistance, inductance, and capacitance of each line are 0.028 Ω/km, 0.553 mH/km, and 20.2 nF/km, respectively. AC grids are fed from the MTDC system via two 400 MW DC to AC converters, namely, Grid Side Converters (GSCs). Two 400 MW Wind farms are supplying the MTDC system of wind power via AC to DC converters, namely, wind side converters (WSCs). This model is built in MATLAB/SIMULINK environment.

The AC currents of all involved converters are controlled to ensure extracting maximum available active power from WSCs, while injecting this power into the involved AC grids with the desired sharing ratios. The power share between the GSCs is achieved by applying droop control. The droop control selects the proper DC voltage reference for each GSC. The AC currents of all converters are controlled by applying dq-current control. The difference between the current control in GSC and WSC is the estimation of direct current reference. For WSCs, the direct current reference is selected based on maximum power point tracking block (MPPT), which is used to generate the proper maximum available power reference (P^*) that can be extracted from the WECS, while the direct current reference at the GSC is selected to ensure that its DC voltage is kept constant at the desired DC voltage reference level. The dq-current control for GSCs and WSCs is shown in Fig. 2.
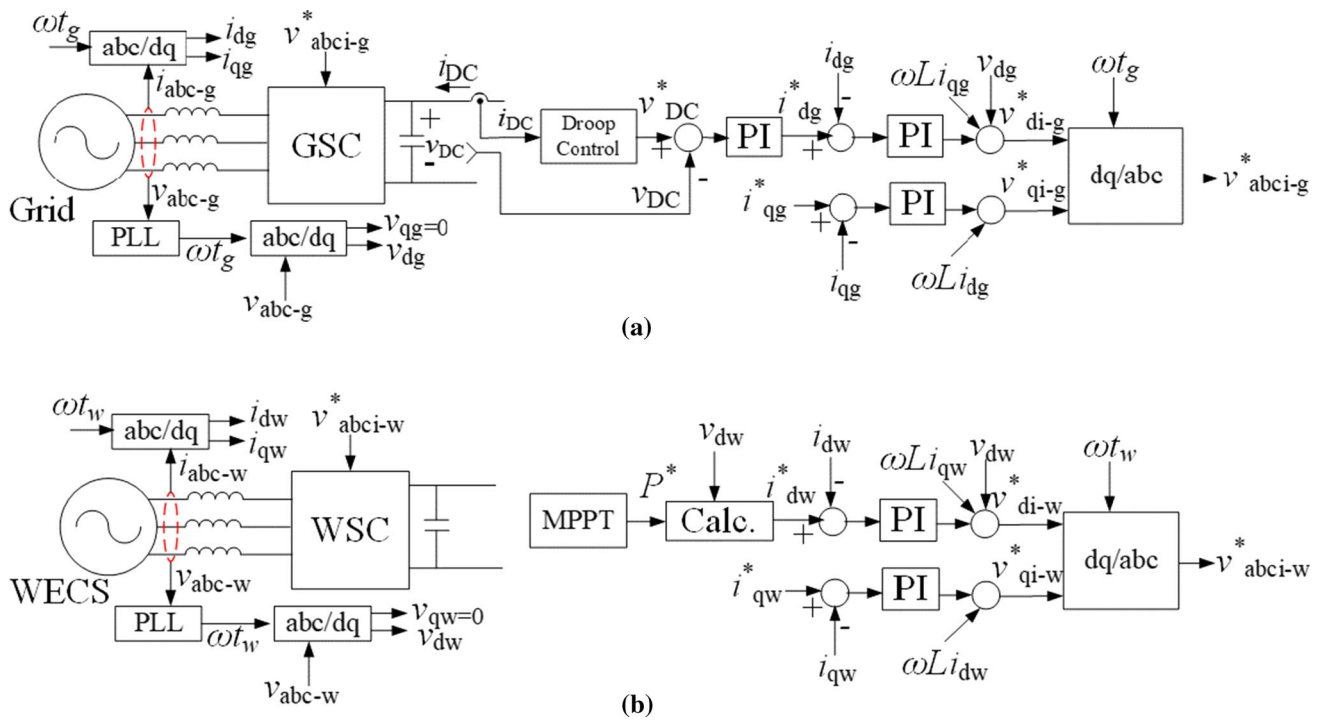
Fig. 2 Current control block diagram of the MTDC converters **a** dq-current control of GSC **b** dq-current control of WSC

The three-phase voltages and currents are transformed into $dq0$ (direct, quadrature, and zero components) coordinates by the Park transformation as in (1);

$$\begin{bmatrix} v_d \\ v_q \\ v_0 \end{bmatrix} = [L] \begin{bmatrix} v_a \\ v_b \\ v_c \end{bmatrix}, \quad \begin{bmatrix} i_d \\ i_q \\ i_0 \end{bmatrix} = [L] \begin{bmatrix} i_a \\ i_b \\ i_c \end{bmatrix} \tag{1}$$

where

$$[L] = \frac{2}{3} \begin{bmatrix} \sin \omega t & \sin\left(\omega t - \frac{2\pi}{3}\right) & \sin\left(\omega t + \frac{2\pi}{3}\right) \\ \cos \omega t & \cos\left(\omega t - \frac{2\pi}{3}\right) & \cos\left(\omega t + \frac{2\pi}{3}\right) \\ \frac{1}{2} & \frac{1}{2} & \frac{1}{2} \end{bmatrix}$$

For given active and reactive power reference, the reference currents in dq-axis, namely, i^*_d and i^*_q are given by (2) and (3) for zero quadrature voltage ($v_q = 0$).

$$i^*_d = \frac{2P^*}{3v_d} \tag{2}$$

$$i^*_q = \frac{2Q^*}{3v_d} \tag{3}$$

where P^* and Q^* are the reference three-phase active and reactive power, respectively, and v_d is the direct voltage.

For GSC, the power is controlled by controlling the reference signal of i^*_d, while the reactive power reference is set to zero, i.e., $i^*_q = 0$. Then the reference current i^*_d is extracted

from the dynamic behavior of the DC link capacitor voltage. To keep DC link capacitor voltage (V_{DC}) constant, the power balance condition should be achieved. The equation is given by (4);

$$\frac{d}{dt} V_{DC}^2 = \frac{2}{C}(P_{in} - P_{out}) \tag{4}$$

where P_{in} is the input power to capacitor, P_{out} is the output power of the DC link capacitor, and C is the capacitance.

Then the reference current i^*_d is extracted from the difference between the actual and reference DC-link voltage as in (5).

$$i^*_d = k_p\left(V_{DC}^* - V_{DC}\right) + \left(k_i \int \left(V_{DC}^* - V_{DC}\right)dt\right) \tag{5}$$

where k_p and k_i are the gains of proportional-integral (PI) controller, and V_{DC}^* is the reference DC-link voltage.

A 15 mH current limiting reactor is inserted at both ends of each line to limit the initial fault current slope to a max of 10 kA/ms for near-bus bolted faults [20]. The value of inductance is selected using trial and error. Figure 3 shows positive pole to ground (p-g) bolted fault in line 1–3 at 1 km from the relay position with and without current limiting reactor. It is clear from Fig. 3a that the fault current increases to extremely high values in a very short period for no reactor case. The fault current slope is around 185.6 kA/ms (fault current increased by 263.61 kA in 1.42 ms) which is a value that cannot be cleared by a regular DC circuit breaker. The
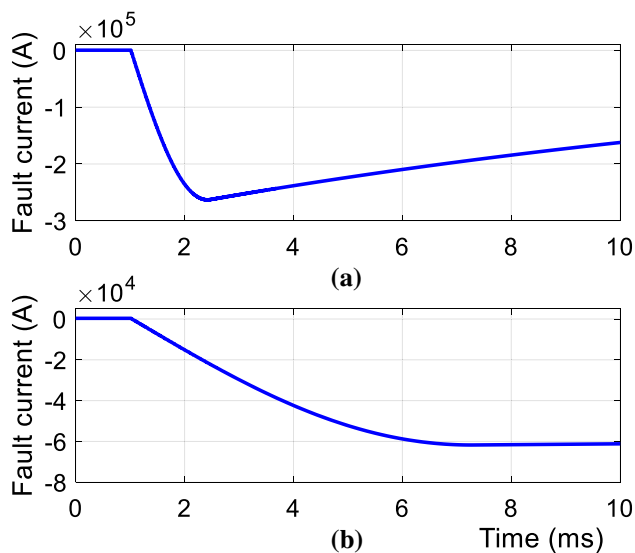
Fig. 3 Comparison between fault current for a bolted positive pole to ground fault in line 1–3 at 3 km from relay location **a** without current limiting inductance **b** with current limiting inductance

Fig. 4 Proposed protection concept **a** internal fault **b** external fault

fault current for the same fault with current limiting reactor is shown in Fig. 3b. It shows that the current slope is reduced very much to an acceptable value of 9.95 kA/ms according to [20] (fault current increased 62.09 kA in 6.24 ms). The selected sampling frequency is 100 kHz, which is enough to capture the needed high frequency transients; therefore, sampling period is 10 μs. This algorithm is single ended algorithm; therefore, no communication is needed. One relay is placed for each line as shown in Fig. 1. All relays are placed near the DC to AC converters.

3 The high frequency-based algorithm

The high frequency-based protection algorithm relies on fault generated high frequency transients. Any fault generates transients that travel along the line to both ends in the form of traveling waves. Part of these traveling waves is reflected to the same line, and the other part passes to other lines. These fault transients can be utilized to identify internal and external faults. For example, a fault in line 1–3 is assumed internal fault to relay R_{13}; nevertheless, it is assumed as external to all relays of other lines. For internal faults, the line relay is exposed to fault transients with all frequencies without any attenuation. For external faults, high frequency transients are attenuated by the busbar stray capacitance, which is very low capacitance that connects busbars to ground [21]. A typical value for this capacitance is 0.1 μF. [21]. The reactance of this stray capacitance is reduced very much at high frequency. Accordingly, it attenuates the high frequency transients generated from an external fault before
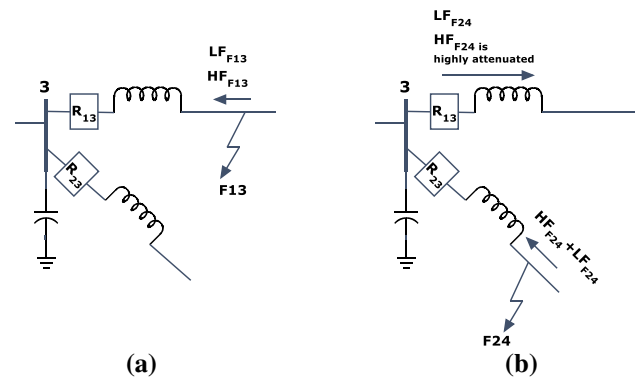
reaching the relay. However, the low frequency transients are slightly affected by this stray capacitance due to its higher reactance. Thus, by calculating the spectral energies of a high frequency and a lower frequency bands, the ratio of the high frequency energy over lower frequency energy will be high in case of an internal fault and low in case of an external fault. This technique is presented before and showed success in case of AC networks [21, 22].

In case of radial MTDC systems, it was proven that the stray capacitance only could not be used to differentiate between internal and external faults [16, 23]. However, in case of meshed MTDC systems, the DC line contains DC current limiters at both ends. These current limiters act as high frequency filters, which will help the stray capacitance to perform the high frequency filtration in case of external fault.

Figure 4 shows a zoom-in for busbar 3 in the model. Two lines are connected to this busbar: line 1–3 and line 2–3. A current limiting reactor is placed at the end of each line as shown in Fig. 4. The reactance of the current limiting reactor is high in case of high frequency transients and low in case of low frequency transients. In case of internal fault, for example fault F13, the relay R_{13} is exposed to low frequency transients (LF_{F13}) and high frequency transients (HF_{F13}) generated form this fault as shown in Fig. 4a. LF_{F13} is minimally affected by the current limiting reactor due to its low reactance. HF_{F13} is affected only by the reactance in line 1–3. Therefore, HF_{F13} will be reduced, but not to very high value. In case of external fault (F24), the fault generated transients will pass through the current limiting reactors of lines 2–4 and 1–3, and pass by the busbar stray capacitance to reach relay R_{13} as shown in Fig. 4b. With respect to HF_{F24}, the high reactance of series current limiting reactors of lines 1–3 and 2–4, and the low reactance of the shunt stray capacitance will highly attenuate HF_{F24} when they reach R_{13}. On the other hand, the low frequency transients of the external fault (LF_{F24}) will reach the relay R_{13} with minimal attenuation due to the low reactance of the series limiting reactors and

the high reactance of the shunt stray capacitance. Accordingly, by calculating the spectral energies contained in high frequency band and low frequency band, the ratio of the high frequency energy to the low frequency energy will be high for internal faults and lower for external faults. This ratio can be used directly to identify internal faults. Therefore, existence of current limiting reactors helps in realization of high frequency-based method presented in Refs. [21, 22] for protection of meshed MTDC systems. Moreover, the conclusion presented in Refs. [16, 23] indicating that the high frequency-based protection method cannot be used for protection of MTDC is correct in case of radial MTDC systems only. However, it will be shown in the simulation results that the high frequency-based protection method can be effectively used for meshed MTDC systems with current limiting reactors.

DWT is a very effective signal processing technique which preserves the time information of a processed signal. DWT is used in this research as a signal processing tool. DWT decomposes the signal into an approximation and several details. Each detail covers a frequency band based on the sampling frequency, i.e., each detail represents a band-pass filter. The selection of mother wavelet depends on the application. There are many orthogonal wavelet families that are suitable for DWT such as Daubichies (db), Symmlets (sym), and Coiflets (coif). The Daubichies (db) family is selected because it has the advantage of asymmetry over the Symmlets and Coiflets. Asymmetry of Daubichies wavelet family makes it suitable for fast fault transients. Daubichies family includes 10 mother wavelets. From db1 (haar) to db10. For short and fast transient disturbances, such as fault transients, mother wavelets such as db4 and db6 are better, while for slower transients, high order mother wavelets such as db8 and db10 are suitable [24]. The mother wavelet db4 showed notable success in different protection algorithms [8, 22, 25]. Accordingly, db4 is used in this study for analysis of fault generated transients.

For 100 kHz sampling frequency, detail1 (d1) coefficients and detail1 (d5) coefficients cover frequency bands of 25–50 kHz and 1.56–3.13 kHz, respectively. These two frequency bands are found suitable for application in the high frequency-based protection algorithm. Coefficients of d1 represent the high frequency band, while coefficients of d5 represent the low frequency band. If the frequency of the high frequency band is increased to increase frequency gap between the two bands, sampling frequency should be increased also. As result, the complexity and cost of application increases. Moreover, this frequency band gives reliable results as evidenced by simulation studies. Furthermore, lowering the frequency of the high frequency band may produce overlap between internal and external faults due to the decreased effect of the busbar capacitance and current limiting reactor. With respect to the low frequency band, taking

lower frequency (higher detail level) is found to be not suitable because it may be affected by other system disturbances or operational issues such as superimposed transients on the main current signal during normal operation. The DC current contains some current ripples, which cannot be removed completely unless extremely high smoothing capacitor is used. On the other hand, increasing the frequency of the low frequency band will have the same effect of reducing the frequency of the high frequency band, which is overlap between internal and external faults.

The energy index of the high frequency band for positive pole is calculated as follows.

$$E_{Hp} = \sum_{c}^{k} d_{1p}^2(k)\Delta t \tag{6}$$

where E_{Hp}: positive pole energy index for the high frequency band, c: an index representing fault detection sample, k: an index representing the ongoing sample, $d_{1p}(k)$: d1 coefficient for positive pole at sample k, and Δt: sampling period.

The same approach is used to calculate the energy index for the low frequency band.

$$E_{Lp} = \sum_{c}^{k} d_{5p}^2(k)\Delta t \tag{7}$$

where E_{Lp}: positive pole energy index for low frequency band, and $d_{5p}(k)$: d5 coefficient for positive pole at sample number k.

Similarly, the high and low energy indices for the negative pole are represented in (8) and (9)

$$E_{Hn} = \sum_{c}^{k} d_{1n}^2(k)\Delta t \tag{8}$$

$$E_{Ln} = \sum_{c}^{k} d_{5n}^2(k)\Delta t \tag{9}$$

The energy ratios are calculated as follows

$$PR = \frac{CO \times E_{Hp}}{E_{Lp}} \tag{10}$$

$$NR = \frac{CO \times E_{Hn}}{E_{Ln}} \tag{11}$$

where PR: the trip ratio for positive pole, NR: the trip ratio for negative pole, and CO: ratio constant.

The ratio of high frequency energy index over low frequency energy index for internal fault is always higher than that for external fault. However, a separating value for the ratio should be identified to differentiate between internal and external faults. The best way to do this is to multiply the

ratio by a constant CO. The philosophy of adding the constant is to keep the ratio above unity for internal faults and below unity for external faults. The transient components are reduced as the frequency increases; therefore, the energy index at high frequency band is lower than that at low frequency band. Accordingly, the constant CO should be larger than unity. These energy indices depend on a large number of factors such as system topology, fault resistance, fault inception time, system parameters, values of current limiting rectors, and distance of fault to the relaying point. Therefore, these energy indices, and subsequently the constant CO, are very difficult to be modeled in a closed form mathematical equation. Alternatively, it is customary to select such ratios based on trial and error [21, 22]. The steps of finding the constant are as follows:

1. Start from a value of CO.
2. Perform multiple simulations for internal fault and external faults under different fault distances covering the whole line length, different fault inception times, different fault resistances, and different fault types.
3. Check if the trip ratios are above unity for all internal faults and below unity for all external faults. If this condition is fulfilled, the CO is final and can be used. If this condition is not fulfilled, adjust CO according to step 4.
4. If the trip ratios for cases of internal faults are blow unity, increase the CO by a value that guarantees that the trip ratio is above unity for all simulated internal faults without affecting the external fault cases. If, on the other hand, the trip ratio for external faults is above unity, this means that the CO is too large. Accordingly, it should be reduced to a level such that the trip ratio is below unity for external faults without affecting the internal fault cases.
5. Re-simulate different external and internal fault cases as explained in step 2. Then, find the trip ratios using the updated CO. If the trip ratios are always above unity for internal faults and below unity for external faults, the CO is final and can be used. If any deviation is found, go to step 4 until finalizing CO.

Based on the aforementioned steps, the constant "CO" is found to be 2000.

A flowchart for the algorithm is shown in Fig. 5. Initially, a 2 ms moving window is loaded with 200 data samples. DWT is performed for positive and negative poles' currents in the window. The window moves sample by sample, and the DWT is performed for each position of the moving window until d1 for positive or negative pole currents exceeds a threshold of 0.5. This threshold is found suitable based on simulations to quickly detect any abnormality. If this threshold is exceeded, a check is done for internal fault. E_{Hp}, E_{Lp} E_{Hn}, E_{Ln}, PR, and NR are calculated according to (10), (11). If PR and NR are lower than unity, the calculation is terminated, and the
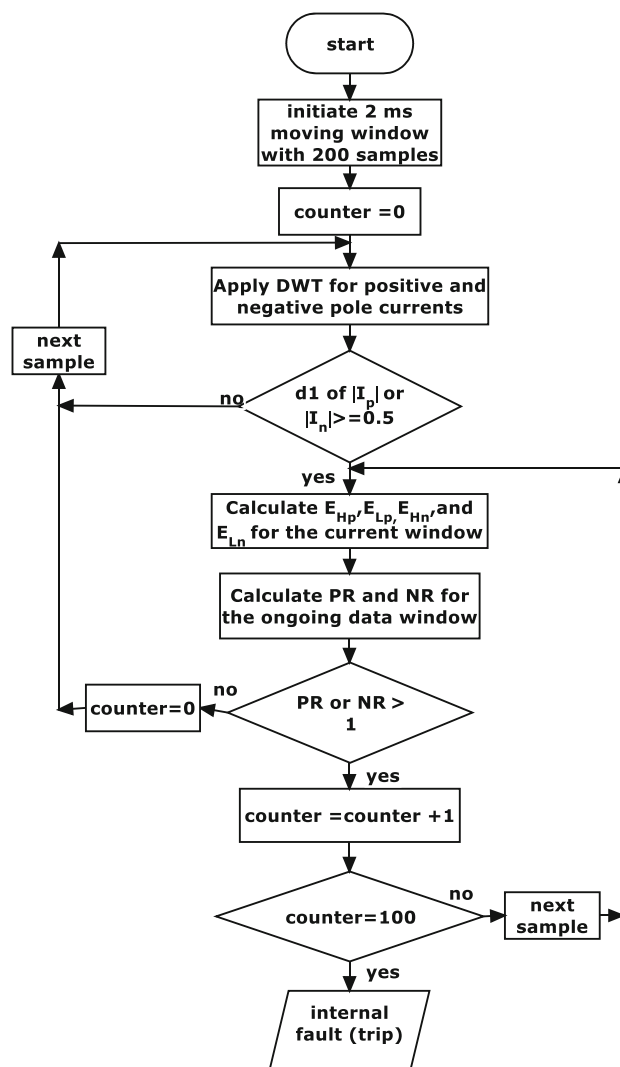

Fig. 5 Flowchart for the high frequency protection algorithm

abnormality is identified as external fault or other external abnormality. The next sample is loaded and whole process restarts again. If PR or NR is larger than unity, an intentional delay is carried out by a counter called trip counter. The trip counter is increased by one and the next sample is loaded, the same process is done for the new window. This delay is necessary to calculate the energy indices and to avoid false tripping.

One hundred samples (1 ms) delay is used to achieve short relaying time. This time delay is within the recommended range of relay operating time for MTDC systems according to [1]. This delay gives reliable results as seen in the performance evaluation. It is worth mentioning that the authors tested other time delays; however, the 1 ms gives excellent results without any overlap between internal and external faults. Accordingly, this time delay is used to achieve full accuracy of the results. If one or both ratios stay over unity
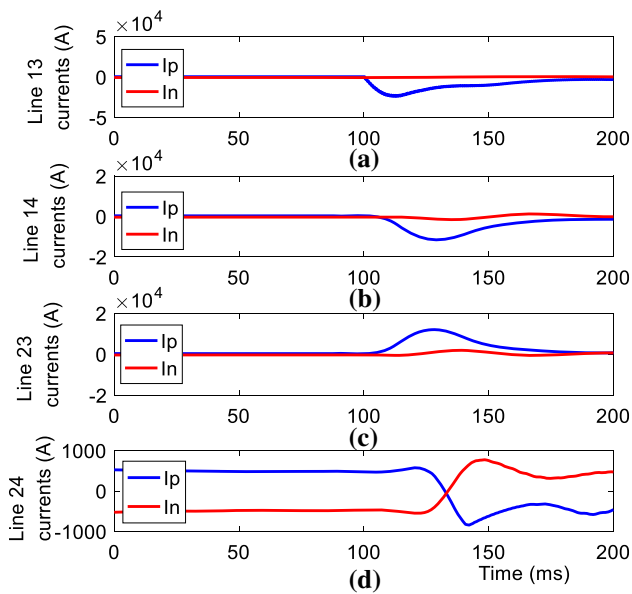
Fig. 6 Positive pole to ground bolted fault in line 1–3 at 100 km from relay position **a** line 1–3 currents **b** line 1–4 currents **c** line 2–3 currents **d** line 2–4 currents
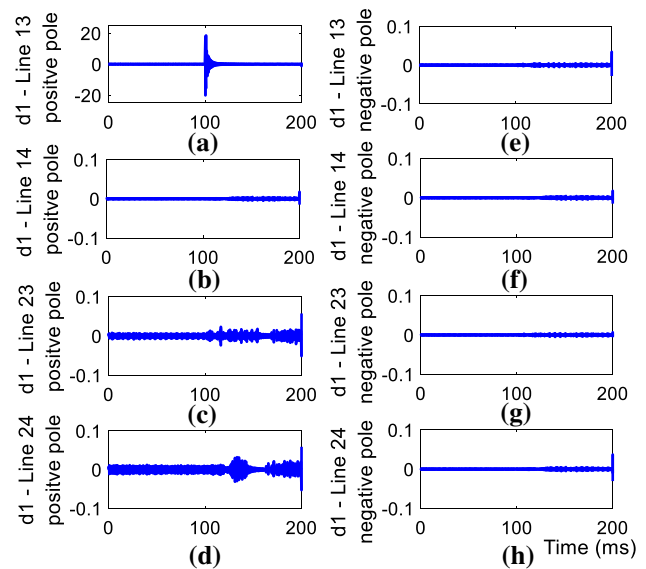

Fig. 7 Detail 1 coefficients for positive pole and negative pole currents for line 1–3 fault **a–d** detail 1 coefficients for positive pole currents **e–h** detail 1 coefficients for negative pole currents
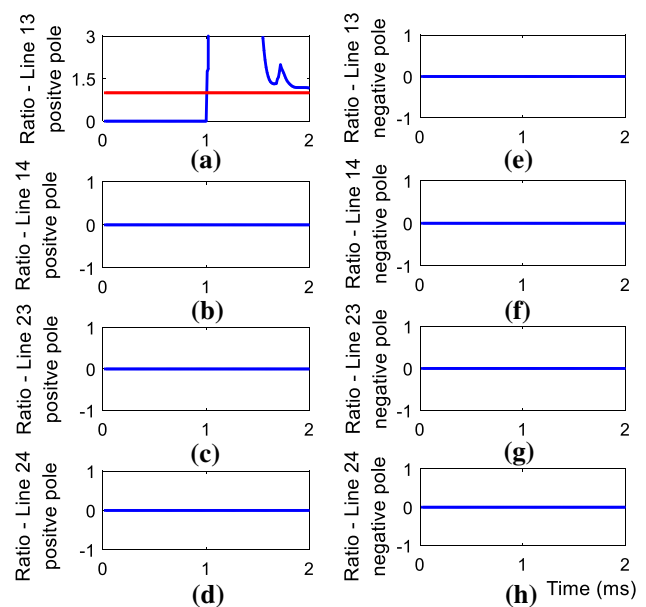
for 100 samples (1 ms), a fault is identified as internal, and a trip signal is issued. If both ratios fall below unity before the counter reaches 100, the fault is identified as external, counter is reset, the next sample is loaded, and the process starts again.

4 Performance evaluation for DC faults

Various faults with different conditions are simulated to verify of the high frequency algorithm. The following subsections illustrate relay responses for a fault in each line.

4.1 A fault in line 1–3

A p-g bolted fault is simulated in line 1–3 at 100 km from relay position (midpoint of the line). Figure 6 shows the positive and negative poles' currents for all lines during this fault. It is evident that the fault current in line 1–3 is the highest among all currents. Figure 7 shows d1 coefficients of both poles' currents for all lines. The d1 coefficients for positive pole current of line 1–3 only exceeded the threshold value, which means that the fault is not even detected in the healthy lines using the used detection threshold. The reason behind that is the extra filtration effect of the current limiting reactors together with the effect of the stray capacitance. This double filtration effect minimizes the high frequency transients of external faults to lower than the fault detection level. This effect appears in case of low values of high frequency components of external fault. Therefore, the energy ratio will be

Fig. 8 Energy ratios for positive pole and negative pole currents for line 1–3 fault at the last window **a–d** ratios for positive pole currents **e–h** ratios for negative pole currents

calculated for positive pole current of line 1–3 only. It is clear from Fig. 8 that the ratio of positive pole of line 1–3 exceeded unity level for the whole intentional delay of 100 samples. The unity level is depicted by the red line. As result, R_{13} issues a trip signal to isolate line 1–3 due to positive pole to ground fault.
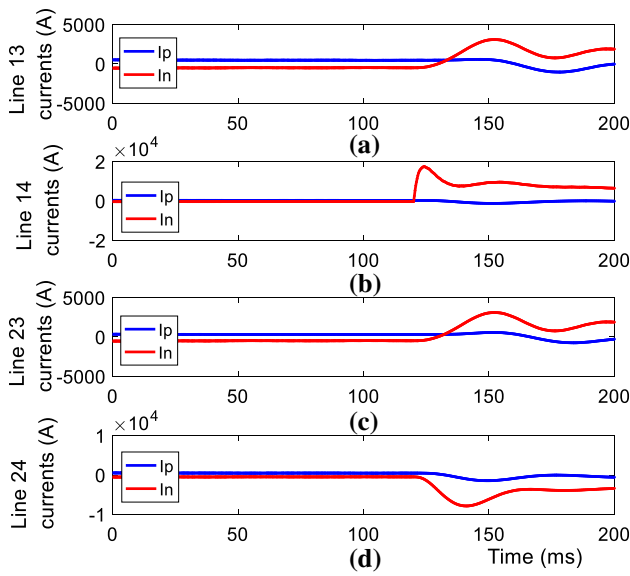
Fig. 9 Negative pole to ground fault in line 1–4 at 10 km from relay position with 10 Ω fault resistance **a** line 1–3 currents **b** line 1–4 currents **c** line 2–3 currents **d** line 2–4 currents
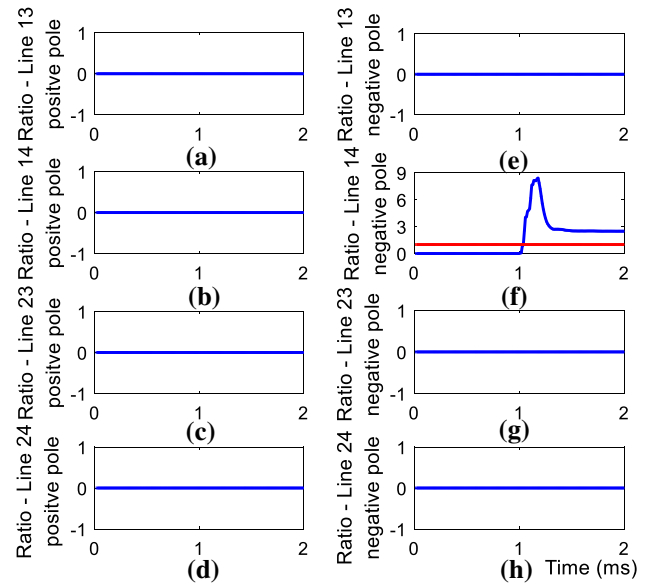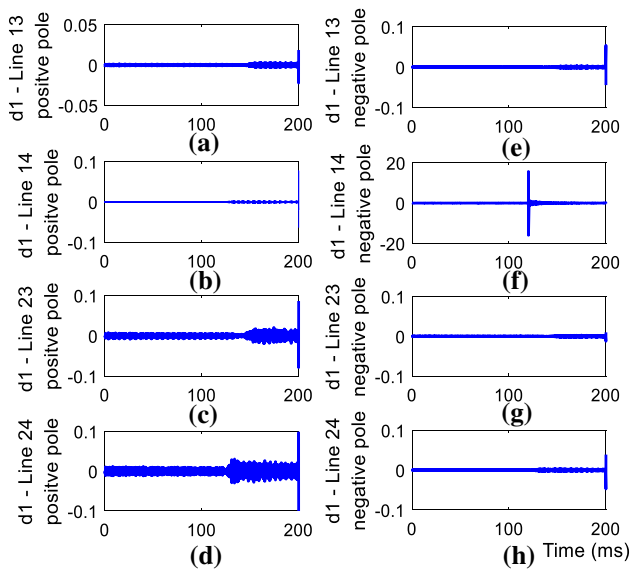

Fig. 10 Detail 1 coefficients for positive pole and negative pole currents for line 1–4 fault **a**–**d** detail 1 coefficients for positive pole currents **e**–**h** detail 1 coefficients for negative pole currents

4.2 A fault in line 1–4

Figure 9 portrays line currents for a negative pole to ground (n-g) fault in line 1–4. The fault is located at 10 km from relay position with 10 Ω fault resistance. This fault is located at 3 percent from the line length. Following the same approach, Figs. 10 and 11 show d1 coefficients for all line currents and the positive and negative energy ratios for all lines at the last window. The fault is detected in line 1–4 only because

Fig. 11 Energy ratios for positive pole and negative pole currents for line 1–4 fault at the last window **a**–**d** ratios for positive pole currents **e**–**h** ratios for negative pole currents

d1 coefficients of the negative pole of line 1–4 exceeded the threshold, whereas d1 of other currents did not. This effect is due to the double filtering effect explained in line 1–3 fault. The trip ratio of the negative pole of line 1–4 remained above unity for 100 samples, which means that a permanent fault occurs in negative pole of line 1–4.

4.3 A fault in line 2–3

A positive pole to negative pole (p-n) fault is simulated in line 2–3. The fault is positioned at 290 km from relay position with 50 Ω fault resistance. This fault is very close to remote bus of the line, as it is located 97 percent from the line length. Figures 12, 13, 14 demonstrate the line currents for the fault, d1 coefficients, and the trip ratios for all lines at the last window. According to performance Figs., the fault is detected in line 2–3 only, and the ratios for both negative and positive poles' currents of line 2–3 exceeded the threshold and remained above unity for the 100 samples. As result, the relay decides a p-n permanent fault in line 2–3.

4.4 A fault in line 2–4

An n-g fault is simulated in line 2–4 at 20 km from relay position. Fault resistance is 100 Ω. Fault currents, detail 1 coefficients, and energy ratios at the last window for all lines are shown in Figs. 15, 16 and 17, respectively. It could be noted that d1 coefficients for negative pole of lines 1–4 and 2–4 passed the threshold. Therefore, the ratios are calculated for negative poles of these lines. Figure 17 indicates that the
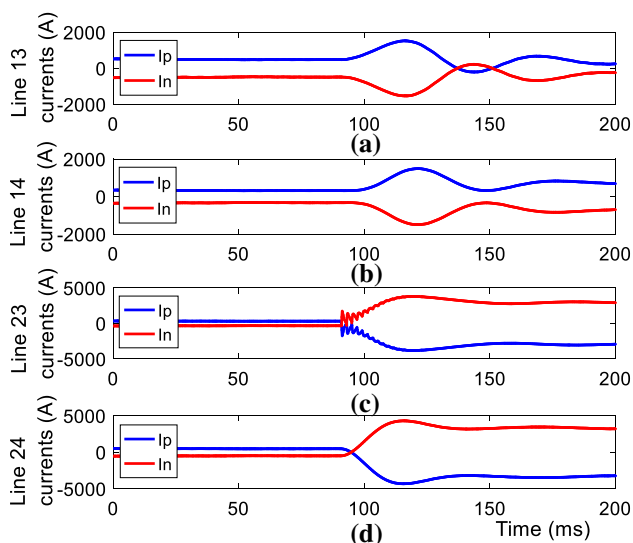
Fig. 12 Positive pole to negative pole fault in line 2–3 at 290 km from relay position with 50 Ω fault resistance **a** line 1–3 currents **b** line 1–4 currents **c** line 2–3 currents **d** line 2–4 currents
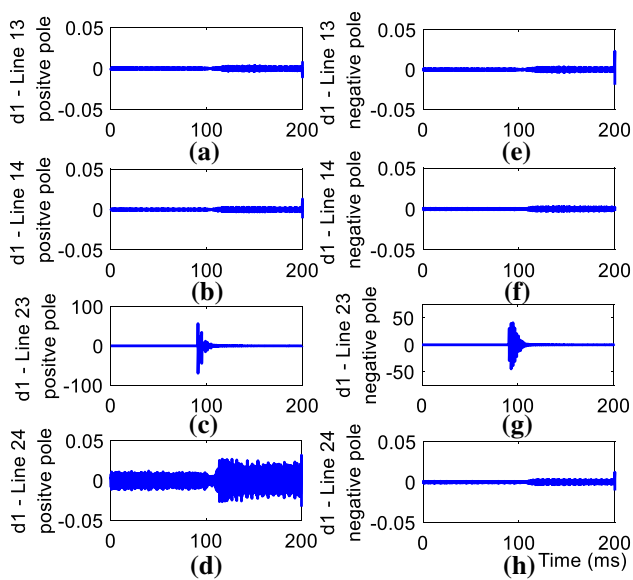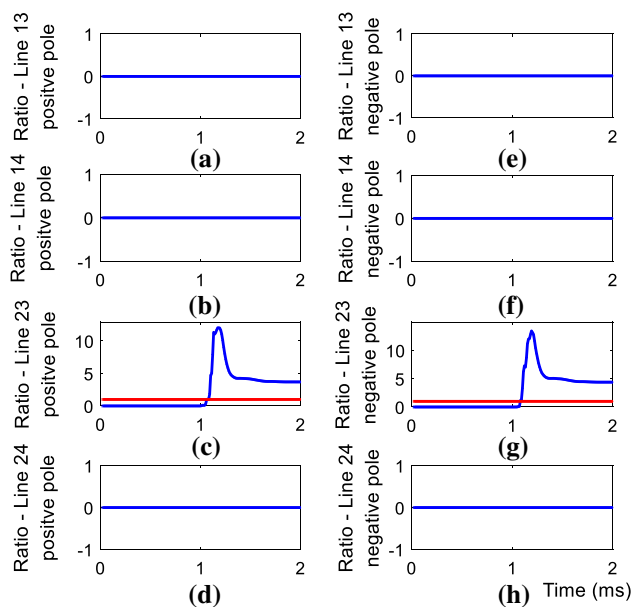

Fig. 13 Detail 1 coefficients for positive pole and negative pole currents for line 2–3 fault **a–d** detail 1 coefficients for positive pole currents **e–h** detail 1 coefficients for negative pole currents

Fig. 14 Energy ratios for positive pole and negative pole currents for line 2–3 fault at the last window **a–d** ratios for positive pole currents **e–h** ratios for negative pole currents
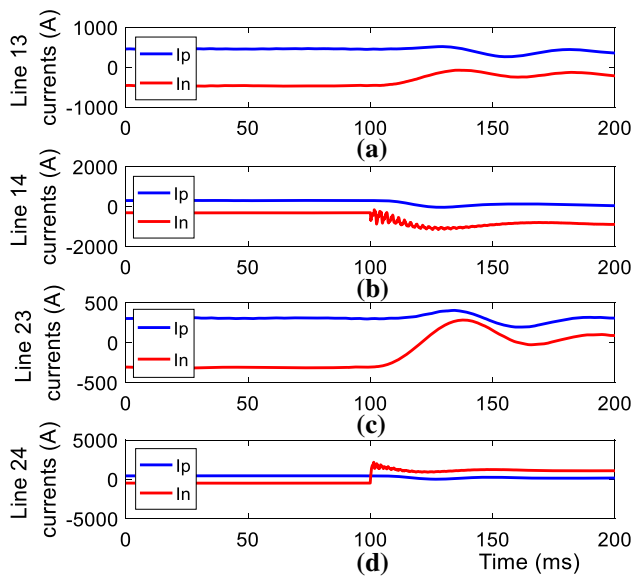

Fig. 15 Negative pole to ground fault in line 2–4 at 20 km from relay position with 100 Ω fault resistance **a** line 1–3 currents **b** line 1–4 currents **c** line 2–3 currents **d** line 2–4 currents

ratio of the negative pole current for line 2–4 passed the unity for the whole period of 100 samples (1 ms). However, the ratio of the negative pole of line 1–4 passed the unity for few samples only (3 samples); then, it dropped below unity for the remaining samples of the intentional delay, which means that no fault in line 1–4. Accordingly, a trip signal is sent to circuit breakers of line 2–4 only due p–n fault. Although d1 coefficients of line 1–4 passed the threshold, the energy ratio of line 2–4 only passed the unity level for whole intentional delay time.

For this particular fault, the negative pole current of line 1–4 has more transients compared to the remaining non-faulty lines. Accordingly, d1 coefficient of this negative pole of this line is the only one which passed the detection threshold. The double filtering effect in this case did not fully absorb the fault generated high frequency transients due to their high level for this particular fault. Although d1 coefficients passed
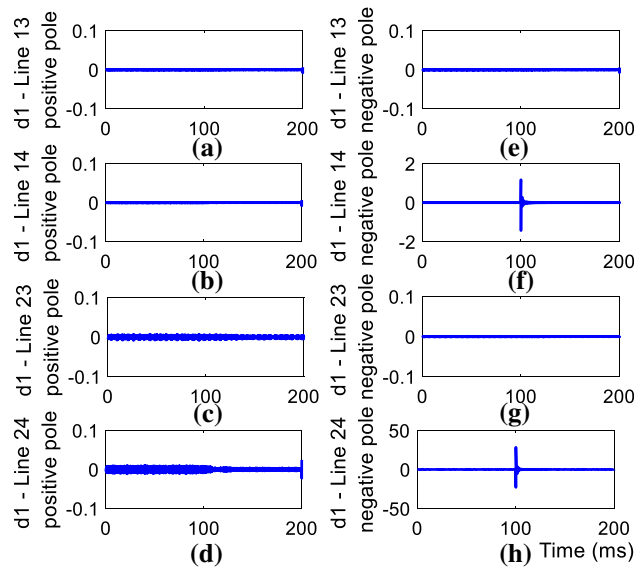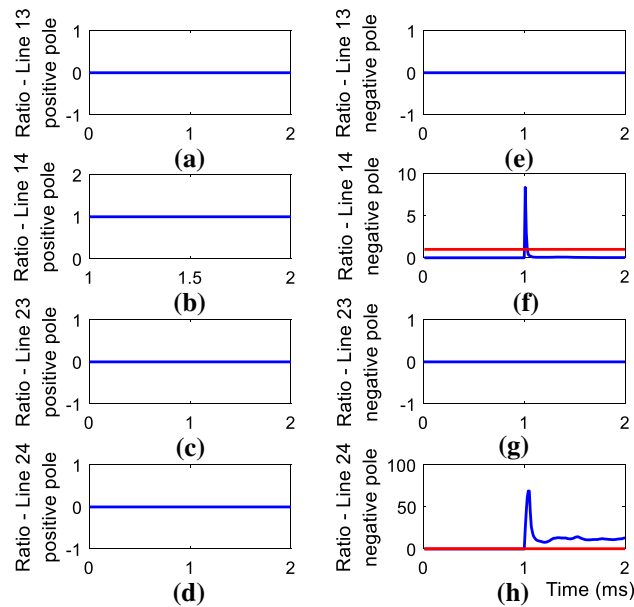
Fig. 16 Detail 1 coefficients for positive pole and negative pole currents for line 2–4 fault **a**–**d** detail 1 coefficients for positive pole currents **e**–**h** detail 1 coefficients for negative pole currents

Fig. 17 Energy ratios for positive pole and negative pole currents for line 2–4 fault at the last window **a**–**d** ratios for positive pole currents **e**–**h** ratios for negative pole currents

the threshold for line 1–4, the trip ratio identifies an internal fault in line 2–4 only.

5 Performance evaluation for other abnormal conditions

This section analyzes the performance of the algorithm against other abnormal conditions such as AC faults and sudden change in the injected wind power. Figure 18 shows the
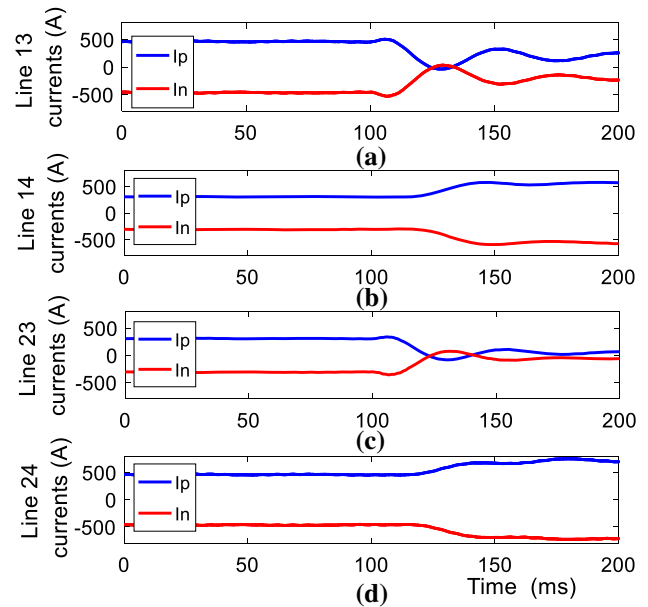
Fig. 18 AC symmetrical bolted fault at the AC side of Grid 1 converter **a** line 1–3 currents **b** line 1–4 currents **c** line 2–3 currents **d** line 2–4 currents
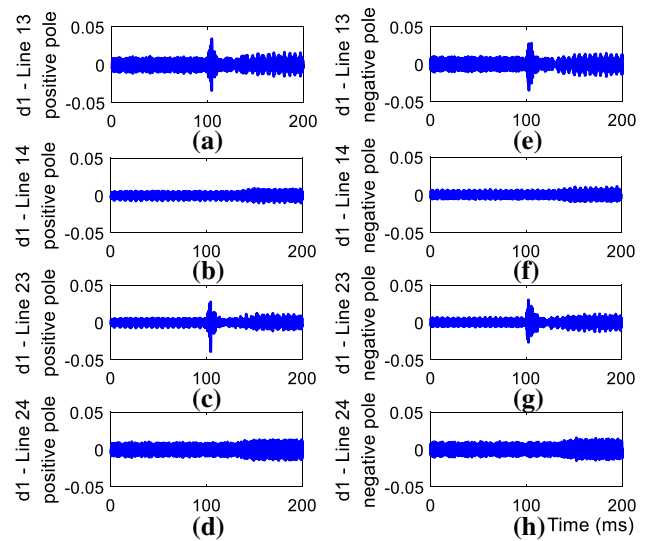

Fig. 19 Detail 1 coefficients for positive pole and negative pole currents for the AC fault **a**–**d** detail 1 coefficients for positive pole currents **e**–**h** detail 1 coefficients for negative pole currents

DC line currents for a three-phase AC fault at grid 1. Figure 19 depicts d1 coefficients for the DC currents. According to Fig. 19, d1 coefficients did not pass the threshold; therefore, trip counters of all relays do not even initiate counting, i.e., no relay in the DC system responds to this abnormality. Figure 20 represents the DC currents for a sudden increase in wind farm 2 power from 200 to 400 MW. This sudden change in the power may cause false tripping for other relaying techniques. However, the relay presented in this paper did not respond to this major abnormality. The coefficients
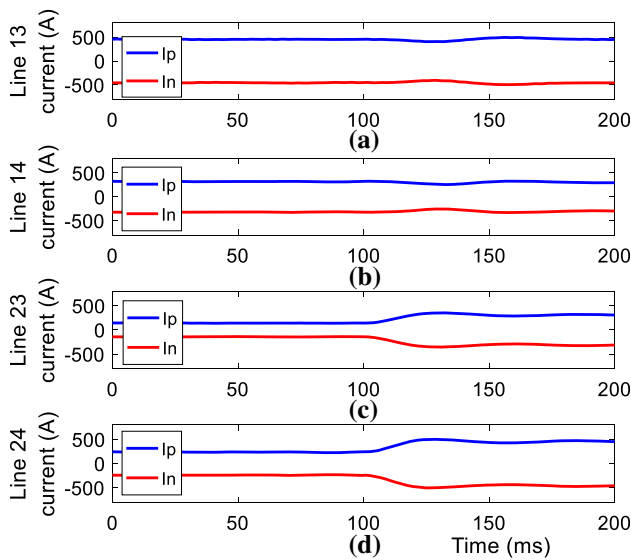
Fig. 20 Step increase of wind farm 2 from 200 to 400 MW **a** line 1–3 currents **b** line 1–4 currents **c** line 2–3 currents **d** line 2–4 currents
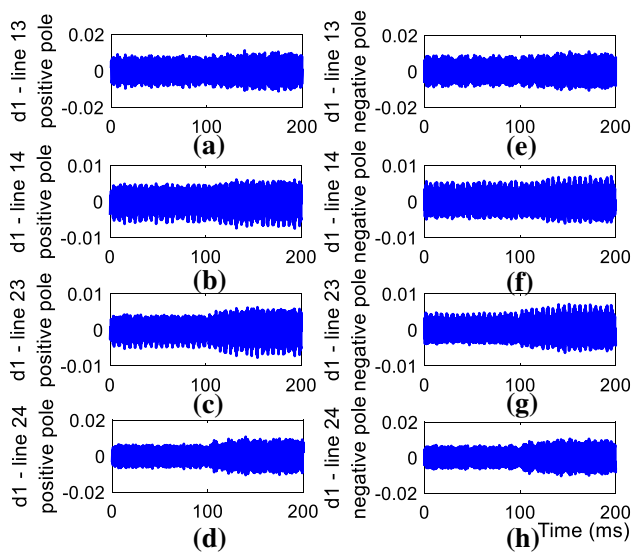

Fig. 21 Detail 1 coefficients for positive pole and negative pole currents for the step power increase **a**–**d** detail 1 coefficients for positive pole currents **e**–**h** detail 1 coefficients for negative pole currents

of d1 of DWT for all DC currents did not pass the threshold as shown in Fig. 21. Accordingly, no fault is detected. The moving window continues to load new samples, and the relay keeps performing fault detection check. Consequently, the algorithm is robust as it does not respond to external abnormalities.

6 Conclusion

A high frequency-based protection algorithm was applied on meshed MTDC system. The current limiting inductors together with the busbar stray capacitance filter the external fault current from its high frequency transients. The filtration effect is much lower for internal faults. The ratio of 1 ms-based energy indices for a high and a low frequency bands was used to classify internal faults. The 1 ms relaying time can be considered as one of the lowest relaying times for protection of MTDC systems. A meshed four-terminal MTDC system with wind farms is used to verify the algorithm. Numerous faults with various conditions and fault resistances were simulated to verify the algorithm. It was found that the high frequency-based algorithm correctly identified all simulated internal faults. Moreover, the relay showed robustness for external abnormal conditions. It did not respond to external DC faults, AC faults, or sudden change in the injected wind power.

References

1. Chaudhuri N, Chaudhuri B, Majumder R, Yazdani A (2014) Multi-terminal direct-current grids: modeling, analysis, and control, 1st edn. Wiley, Hoboken
2. Abdel-Khalik AS, Massoud AM, Elserougi AA, Ahmed S (2013) Optimum power transmission-based droop control design for multi-terminal HVDC of offshore wind farms. IEEE Trans Power Syst 28:3401–3409
3. Dierckxsens C, Srivastava K, Reza M, Cole S, Beerten J, Belmans R (2012) A distributed DC voltage control method for VSC MTDC systems. Electr Power Syst Res 82:54–58
4. Chaudhuri NR, Chaudhuri B (2013) Adaptive droop control for effective power sharing in multi-terminal DC (MTDC) grids. IEEE Trans Power Syst 28:21–29
5. Xydis G (2013) Comparison study between a renewable energy supply system and a supergrid for achieving 100% from renewable energy sources in Islands. Int J Electr Power Energy Syst 46:198–210

6. Jin Y, Fletcher JE, O'Reilly J (2010) Multiterminal DC wind farm collection grid internal fault analysis and protection design. IEEE Trans Power Delivery 25:2308–2318

7. De Kerf K, Srivastava K, Reza M, Bekaert D, Cole S, Van Hertem D, Belmans R (2011) Wavelet-based protection strategy for DC faults in multi-terminal VSC HVDC systems. IET Gener Transm Distrib 5:496–503

8. Sabug L, Musa A, Costa F, Monti A (2020) Real-time boundary wavelet transform-based DC fault protection system for MTDC grids. Int J Electr Power Energy Syst 115:105475

9. Li Y, Gong Y, Jiang B (2018) A novel traveling-wave-based directional protection scheme for MTDC grid with inductive DC terminal. Electr Power Syst Res 157:83–92

10. Liu L, Liu Z, Popov M, Palensky P, Meijden MAMMVD (2021) A fast protection of multi-terminal HVDC system based on transient signal detection. IEEE Trans Power Delivery 36:43–51

11. Abu-Elanien AEB, Elserougi AA, Abdel-Khalik AS, Massoud AM, Ahmed S (2016) A differential protection technique for multi-terminal HVDC. Electr Power Syst Res 130:78–88

12. Azizi S, Afsharnia S, Sanaye-Pasand M (2014) Fault location on multi-terminal DC systems using synchronized current measurements. Int J Electr Power Energy Syst 63:779–786

13. Tong N, Lin X, Li Y, Hu Z, Jin N, Wei F, Li Z (2019) Local measurement-based ultra-high-speed main protection for long distance VSC-MTDC. IEEE Trans Power Delivery 34:353–364

14. Cheng J, Guan M, Tang L, Huang H (2014) A fault location criterion for MTDC transmission lines using transient current characteristics. Int J Electr Power Energy Syst 61:647–655

15. Raza A, Akhtar A, Jamil M, Abbas G, Gilani SO, Yuchao L, Khan MN, Izhar T, Dianguo X, Williams BW (2018) A protection scheme for multi-terminal VSC-HVDC transmission systems. IEEE Access 6:3159–3166

16. Abu-Elanien AEB, Abdel-Khalik AS, Massoud AM, Ahmed S (2017) A non-communication based protection algorithm for multi-terminal HVDC grids. Electric Power Systems Research 144:41–51

17. Abu-Elanien AEB (2018) Protection of star connected multi-terminal HVDC systems with offshore wind farms. In: 2018 IEEE 12th international conference on compatibility, power electronics and power engineering (CPE-POWERENG 2018), Doha, Qatar, pp 1–6

18. Abu-Elanien AEB (2019) An artificial neural network based technique for protection of HVDC grids. In: 2019 IEEE PES GTD grand international conference and exposition Asia (GTD Asia), Bangkok, Thailand, pp 1004-1009

19. Yang Q, Le Blond S, Aggarwal R, Wang Y, Li J (2017) New ANN method for multi-terminal HVDC protection relaying. Electr Power Syst Res 148:192–201

20. Leterme W, Beerten J, Hertem DV (2016) Nonunit protection of HVDC grids with inductive DC cable termination. IEEE Trans Power Delivery 31:820–828

21. Bo ZQ (1998) A new non-communication protection technique for transmission lines. IEEE Trans Power Delivery 13:1073–1078

22. Megahed AI, Moussa AM, Bayoumy AE (2006) Usage of wavelet transform in the protection of series-compensated transmission lines. IEEE Trans Power Delivery 21:1213–1221

23. Zhang S, Zhang BH, You M, Bo ZQ (2010) Realization of the transient-based boundary protection for HVDC transmission lines based on high frequency energy criteria. In: 2010 International conference on power system technology (POWERCON), Zhejiang, China, pp 1–7

24. Santoso S, Powers EJ, Grady WM, Hofmann P (1996) Power quality assessment via wavelet transform analysis. IEEE Trans Power Delivery 11:924–930

25. Lin S, Gao S, He Z, Deng Y (2015) A pilot directional protection for HVDC transmission line based on relative entropy of wavelet energy. Entropy 17:5257–5273